

## Impact of further-range exchange and cubic anisotropy on magnetic excitations in the fcc kagome antiferromagnet $\text{IrMn}_3$

M. D. LeBlanc,<sup>1</sup> A. A. Aczel,<sup>2</sup> G. E. Granroth,<sup>2</sup> B. W. Southern,<sup>3</sup> J.-Q. Yan,<sup>4</sup> S. E. Nagler,<sup>2</sup>  
J. P. Whitehead,<sup>1</sup> and M. L. Plumer<sup>1</sup>

<sup>1</sup>*Department of Physics and Physical Oceanography, Memorial University of Newfoundland, St. John's, Newfoundland, A1B 3X7, Canada*

<sup>2</sup>*Neutron Scattering Division, Oak Ridge National Laboratory, Oak Ridge, Tennessee 37831, USA*

<sup>3</sup>*Department of Physics and Astronomy, University of Manitoba, Winnipeg, MB, R3T 2N2, Canada*

<sup>4</sup>*Materials Science and Technology Division, Oak Ridge National Laboratory, Oak Ridge, Tennessee 37831, USA*



(Received 13 July 2018; revised 25 May 2021; accepted 8 July 2021; published 27 July 2021)

This work investigates the effects of further neighbor exchange and cubic anisotropy on the magnetic excitations of the fcc kagome antiferromagnet  $\text{IrMn}_3$ . Spin wave frequencies are calculated using the torque equation and the dynamical structure factor  $S(\mathbf{Q}, \omega)$  is determined by a Green's function method as an extension of our previous work [LeBlanc *et al.* *Phys. Rev. B* **90**, 144403 (2014)]. These spin wave calculations are compared with inelastic neutron scattering data of polycrystalline  $\text{IrMn}_3$ , where magnetic Mn ions occupy lattice sites of ABC-stacked kagome planes. The data are best explained by a spin wave model including exchange interactions up to fourth nearest neighbor and strong cubic anisotropy, as previously predicted by density functional theory calculations.

DOI: [10.1103/PhysRevB.104.014427](https://doi.org/10.1103/PhysRevB.104.014427)

### I. INTRODUCTION

$\text{IrMn}_3$  provides an important example of a truly three-dimensional (3D) kagome lattice giving rise to geometrical magnetic frustration from eight nearest neighbor (NN) antiferromagnetic exchange interactions between Mn ions [1]. ABC stacking of kagome planes of Mn ions in the cubic (111) directions gives an overall  $\text{L1}_2$ ,  $\text{AuCu}_3$ -type, fcc structure with four NNs within each plane and two NNs connecting each adjacent plane (see Fig. 1). Interest in the magnetic properties of the corresponding two-dimensional (2D) kagome NN Heisenberg antiferromagnet spans 25 years due to the macroscopic spin degeneracy of the basic  $120^\circ$  spin structure associated with corner-sharing triangles [2]. The zero energy dispersionless (flat) spin wave mode at all wave vectors predicted from classical theory acquires dispersion in the presence of further-neighbor exchange interactions [3,4]. Inelastic neutron scattering (INS) data on a system with weakly-coupled kagome planes appear consistent with this scenario where the flat mode observed is gapped due to additional Dzyaloshinskii-Moriya interactions [5].

Interest in  $\text{IrMn}_x$  alloys over the past 15 years has mainly arisen due to applications in spin-valve technology, where they have been widely used as the antiferromagnetic thin film of choice that pins the magnetic moments of an adjacent ferromagnet in the phenomenon known as exchange bias [6–9]. Although there is no universally accepted microscopic mechanism for exchange bias (pinning), magnetic frustration is believed to be important as the pinning effect arises from a field-cooling protocol where a desired metastable state, among many nearly degenerate states, is stabilized. Stoichiometric  $\text{IrMn}_3$  appears to optimize the desired pinning [7].

Monte Carlo simulations of the NN Heisenberg fcc kagome lattice have shown that the basic co-planar  $120^\circ$   $q = 0$  magnetic structure observed in 2D persists in the 3D case, with the inter-spin angle being  $120^\circ$  between all eight NNs (shown in Fig. 1) [1]. The spin degeneracy is reduced in 3D and exists in the form of sublattice magnetization switching in the stacked kagome planes. This persistent degeneracy is believed to be responsible for the first-order nature of the phase transition at  $T_N$ . Inspired by earlier electronic structure calculations [10], subsequent simulations of the 3D lattice with an effective local cubic anisotropy included provided evidence that anisotropy removes the basic kagome degeneracy and the structure becomes non coplanar with a finite magnetization (spin vectors are lifted out of the [111] plane), believed to be important for the pinning of an adjacent ferromagnetic layer in the spin-valve structure. This release of frustration drives the transition to be continuous [11]. This scenario was supported by spin wave calculations of the NN Heisenberg model with and without anisotropy which demonstrated that in the absence of anisotropy, the zero energy flat mode exists only in certain high symmetry directions in reciprocal space and that the addition of anisotropy induces a gap (Ref. [12], hereafter referred to as I). Monte Carlo studies of [111] thin films confirmed that the  $q = 0$  magnetic order remains in these geometries and the impact of surface axial anisotropy was also considered [13].

Early neutron scattering experiments on sister compounds  $\text{RhMn}_3$  and  $\text{PtMn}_3$  revealed the  $120^\circ$  magnetic order [14] which was subsequently established in single crystal neutron scattering studies on  $\text{IrMn}_3$  by Tomeno *et al.* [15] and referred to as “T1” magnetic order, with no mention of the underlying kagome lattice structure of magnetic ions or any indication of

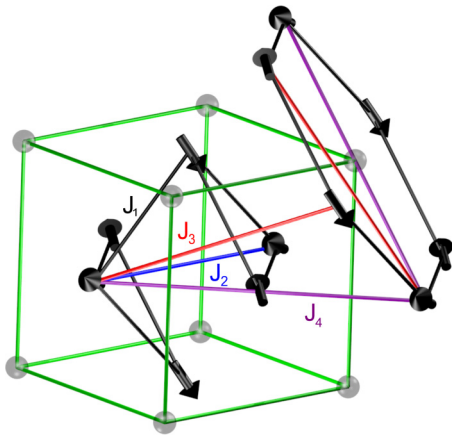


FIG. 1. ABC-stacked kagome planes forming the fcc kagome lattice with magnetic ions occupying the face-centered cubic sites. Illustrated are spin vectors forming the  $120^\circ q = 0$  [111] planar spin structure (zero anisotropy) and the exchange interactions  $J_1$ ,  $J_2$ ,  $J_3$ , and  $J_4$ .

a finite magnetization. More recently, single crystal [111] thin films of  $\text{IrMn}_3$  showed the same magnetic order as in the bulk where exchange bias was also studied [8]. To our knowledge, there have been no neutron scattering experiments reporting on spin excitations in these magnetic fcc kagome systems. It is of interest to note another class of Mn-based compounds with the generic formula  $\text{Mn}_3\text{AX}$  also exhibits fcc kagome magnetism [16].

The high Néel temperature in  $\text{IrMn}_3$ ,  $T_N \simeq 960$  K (with large values also reported in the sister compounds), attractive for device applications, can be associated with large exchange interactions. For example, an antiferromagnetic NN  $S^2J_1 = 20.6$  meV ( $J_1 = 11.6$  meV) has been estimated for  $\text{IrMn}_3$  from the density functional theory (DFT) calculations by Szunyogh *et al.* [10], where an effective spin  $S = 1.33$  has been folded into the reported exchange constant values [10,17]. This and related work also reported substantial longer-range exchange interactions of an oscillatory nature, with  $S^2J_2 = -2.6$  meV ( $J_2 = -1.5$  meV),  $S^2J_3 = 5.6$  meV ( $J_3 = 3.2$  meV),  $S^2J_4 = -2.5$  meV ( $J_4 = -1.4$  meV), as well as a large effective cubic anisotropy [18]  $S^2K_{\text{eff}} \simeq 7.67$  meV (see Table I). The DFT results indicate that longer-range exchange interactions beyond fourth neighbor are negligibly small [10]. Analysis shows that these longer-range alternating antiferromagnetic and ferromagnetic exchange interactions are consistent with the 3D  $q = 0$  spin structure and do not introduce additional frustration. A first-principles molecular spin dynamics study of  $\text{PtMn}_3$  and  $\text{RhMn}_3$  also reports enhanced second-neighbor exchange interactions [19].

In the present work, the nearest neighbor spin wave calculations reported in I are expanded to include further-neighbor exchange  $J_2$ ,  $J_3$ , and  $J_4$ . As in the 2D case, these additional interactions remove any flat modes and dispersion appears in all cases. The impact of cubic anisotropy  $K$  is again examined in the presence of the additional exchange interactions. The dynamical structure factor,  $S(\mathbf{Q}, \omega)$ , is calculated for both single crystal and powder sample scenarios. Results are compared with inelastic neutron scattering data on powder

TABLE I. Exchange parameters for the fcc kagome lattice  $\text{IrMn}_3$  (see Fig. 1) where  $J > 0$  implies antiferromagnetic coupling. DFT values are taken from Ref. [10] and the factor of two reduction here arises from the difference in the Hamiltonian definitions of the previous and current work. Distances are relative to the lattice constant  $a = 3.76$  Å [15].

| Exchange Interactions in $\text{IrMn}_3$ |                               |           |                               |           |
|--|-------------------------------|-----------|-------------------------------|-----------|
| nth Near Neighbor                        | $S^2J_1$                      | $S^2J_2$  | $S^2J_3$                      | $S^2J_4$  |
| Value from DFT (meV)                     | 20.6                          | -2.6      | 5.6                           | -2.5      |
| Neighbors in plane                       | 4                             | 0         | 4                             | 6         |
| Neighbors first adjacent planes          | 4                             | 6         | 8                             | 0         |
| Neighbors second adjacent planes         | 0                             | 0         | 4                             | 6         |
| Total                                    | 8                             | 6         | 16                            | 12        |
| Vector                                   | $[\frac{1}{2} \frac{1}{2} 0]$ | $[1 0 0]$ | $[1 \frac{1}{2} \frac{1}{2}]$ | $[1 1 0]$ |
| Distance ( $a$ )                         | 0.707                         | 1         | 1.225                         | 1.414     |

samples of  $\text{IrMn}_3$  with the ordered  $\text{AuCu}_3$  structure. The effects of further-order exchange are demonstrated to be important. Furthermore, the observation of a large spin gap in the INS data is important experimental evidence for strong cubic anisotropy in this material and suggests that the coplanar magnetic structure previously reported [15] should be revisited.

## II. MODEL RESULTS

Modifications to our previous analysis in I to include further-neighbor exchange interactions are described here, with details given in Appendix A. In that work,  $J$  represented the NN exchange in kagome planes and  $J'$  denoted NN inter-plane exchange. Here, we set  $J_1 = J = J'$ . The  $120^\circ q = 0$  spin structure is characterized by three magnetic sublattice magnetization vectors labeled as A, B, and C, and we consider the following Hamiltonian:

$$\mathcal{H} = \sum_{i,j} J(|\mathbf{r}_i - \mathbf{r}_j|) \mathbf{S}_i \cdot \mathbf{S}_j - K \sum_{\gamma} \sum_{l \subset \gamma} (\mathbf{S}_l \cdot \mathbf{n}_{\gamma})^2. \quad (1)$$

Note that [11]  $K = \frac{1}{2}K_{\text{eff}} \geq 0$  has a different easy direction for each of the three sublattices. Here,  $\gamma$  represents sublattice A, B, and C and  $l$  is summed over the  $\frac{N}{3}$  spins of sublattice  $\gamma$ ,  $\mathbf{S}_l$  are unit classical Heisenberg spin vectors at each site and  $\mathbf{n}_{\gamma}$  are unit vectors in the cubic axes directions,  $\mathbf{n}_A = \hat{\mathbf{x}}$ ,  $\mathbf{n}_B = \hat{\mathbf{y}}$ , and  $\mathbf{n}_C = \hat{\mathbf{z}}$ . The lattice constant of ordered  $\text{IrMn}_3$  has been determined at room temperature to be  $a = 3.76$  Å [15]. The Mn ions occupy face-centered-cubic sites, with  $\gamma = A$  at  $[0, \frac{1}{2}, \frac{1}{2}]$ ,  $\gamma = B$  at  $[\frac{1}{2}, 0, \frac{1}{2}]$ , and  $\gamma = C$  at  $[\frac{1}{2}, \frac{1}{2}, 0]$ , separated by a distance  $a/\sqrt{2} = 2.67$  Å as depicted in Fig. 1. The model results presented below include magnetic anisotropy and exchange constants up to fourth nearest-neighbor, with values used for the latter given in Table I. In order to demonstrate the impact of these further-neighbor exchange interactions, as well as anisotropy, we also consider model results with some of the exchange constants or the magnetic anisotropy set to zero.

Figure 2 shows the spin wave frequencies  $\omega$  along the  $\Gamma X(100)$ ,  $\Gamma M(110)$  and  $\Gamma R(111)$  directions with only NN exchange  $J_1$  included and also with further-neighbor  $J_2$ ,  $J_3$ , and  $J_4$  added, with and without cubic anisotropy  $K$  (also

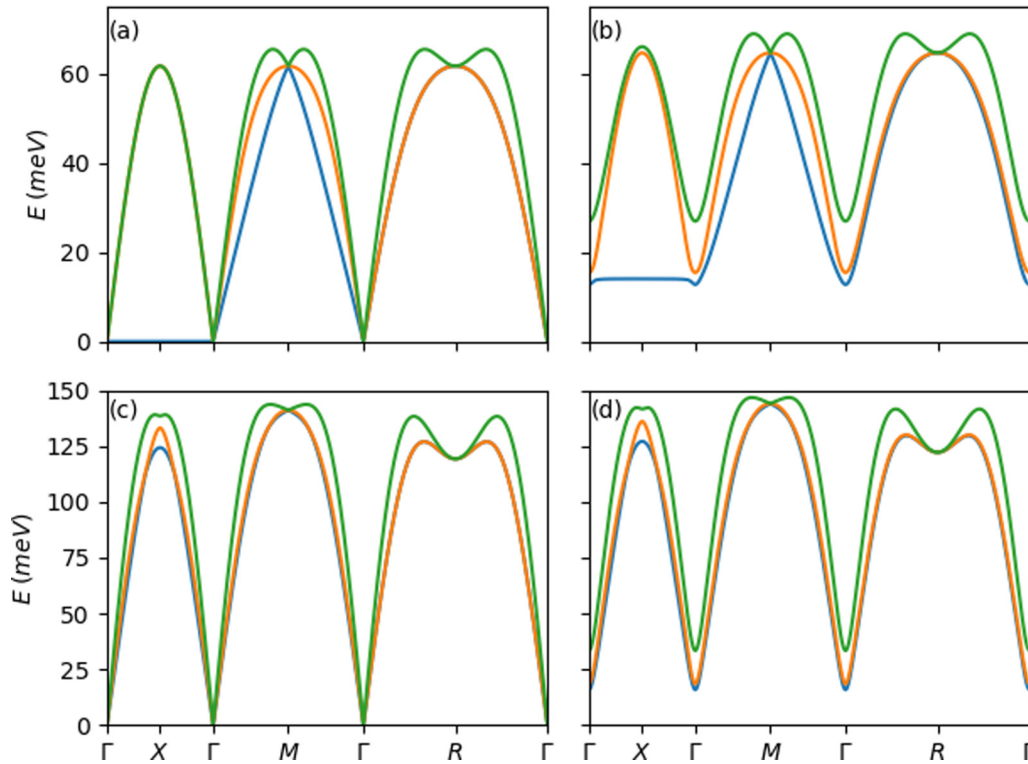


FIG. 2. Spin wave modes along the  $\Gamma X$ ,  $\Gamma M$  and  $\Gamma R$  directions, illustrating the impact of anisotropy and further-neighbor exchange interactions, for (a) NN exchange only and  $K = 0$ , (b) NN exchange only and  $K = 2.2$  meV, (c) exchange interactions up to 4NN and  $K = 0$ , and (d) exchange interactions up to 4NN and  $K = 2.2$  meV. As shown in (a), there is a zero energy mode along  $\Gamma X$  (blue line) and the remaining two modes (orange and green lines) are degenerate. Exchange constant values from the DFT calculation listed in Table I were used to generate these dispersion curves.

see I). The effect of further-neighbor interactions is to lift the degeneracy that gives rise to the flat zero energy mode (blue line) that occurs along  $\Gamma X$  with only NN interactions, as shown in Figs. 2(a) and 2(c). The resulting dispersion of this mode is now nearly the same as the other two branches. Note as well that the degeneracy of the other two modes (orange and green lines) occurring around the  $X$  point in the case of only NN exchange is split with longer-range interactions included. As before, the impact of anisotropy  $K > 0$  is to introduce a gap at the zone center as shown in Figs. 2(b) and 2(d). Also note that two of the modes along the  $\Gamma$ - $M$  line are degenerate with further-neighbor exchange added [blue and orange lines in Figs. 2(c) and 2(d)] that were well separated with only NN interactions [Figs. 2(a) and 2(b)]. In contrast, the near-degeneracy of these modes around the  $R$  point is hardly impacted by including further-neighbor exchange. At the zone center  $\mathbf{q} = \mathbf{0}$ , the frequencies of the modes for the extended neighbor exchange model with cubic anisotropy are given by

$$\begin{aligned}\omega_1 &\simeq \omega_2 \simeq 2S\sqrt{(J_1 + 2J_3)K}, \\ \omega_3 &\simeq 4S\sqrt{(J_1 + 2J_3)K}.\end{aligned}\quad (2)$$

The DFT values described above therefore lead to spin gap predictions of about 17 and 33 meV, respectively, for  $\text{IrMn}_3$ .

The Green's function method [20] used in I was applied here to calculate the part of the dynamical structure factor that

contributes to the inelastic neutron scattering cross section

$$S(\mathbf{Q}, \omega) = \sum_{m,n=x,y,z} S^{mn}(\mathbf{Q}, \omega)(\delta_{mn} - \hat{Q}_m \hat{Q}_n) \quad (3)$$

where  $S^{mn}(\mathbf{Q}, \omega)$  is the double Fourier transform of the correlation function  $\langle S_i^m(0)S_j^n(t) \rangle$ , to provide an indication of the inelastic neutron scattering response for  $\text{IrMn}_3$  with all four NN exchange interactions and anisotropy included.

Figure 3 shows  $S(\mathbf{Q}, \omega)$  assuming a single magnetic (111) domain for  $\mathbf{Q}$  along the three principal cubic directions with further-neighbor exchange as well as anisotropy included. Corresponding results with only NN exchange and  $K$  included for  $\mathbf{Q}$  along [100] may be found in I. Of particular note is that for the cases with  $\mathbf{Q}$  along [100] and [110], the intensity is expected to be relatively small in the first Brillouin zone but is substantially larger in the second zone. This is not the case for  $\mathbf{Q}$  along [111] but the overall intensity is much weaker for the wave vector in this direction.

Figure 3 can be compared with Fig. 2(d), illustrating the removal of the low-frequency mode along  $\Gamma X$  with the addition of extra neighbors and the splitting of the degeneracy of the higher frequency modes. Noticeably, along the [111] direction there is a mode not seen in Fig. 3 that is present in Fig. 2(d). This is not an added degeneracy, but is rather due to a perfect cancellation in intensity when applying Eq. (3). A similar effect is observed in the elastic scattering results of Fig. 3 of I where there is no peak at [111] unless anisotropy is added.

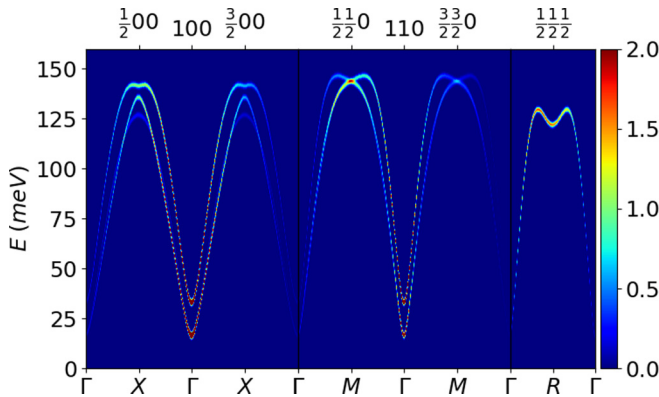


FIG. 3. Dynamical structure factor  $S(\mathbf{Q}, \omega)$  for  $\text{IrMn}_3$  assuming a single magnetic (111) domain along the three principal cubic directions. Indicated wave vectors show the symmetric points in the dispersion. Exchange constant values given in Table I and a magnetic anisotropy of  $K = 2.2$  meV were used to generate this plot.

### III. INELASTIC NEUTRON SCATTERING

#### A. Motivation and sample preparation

We performed inelastic neutron scattering (INS) on polycrystalline  $\text{IrMn}_3$  to test the validity of the magnetic Hamiltonian determined by DFT calculations previously [10,18]. To prepare polycrystalline  $\text{IrMn}_3$ , Mn, and Ir powders in the molar ratio of 3:1 were first mixed well and pelletized. The pellets were then sealed inside of a quartz tube under approximately 1/3 atmosphere of argon gas. The sealed ampoule was heated to 1050 °C in 10 hours and kept at this temperature for 48 hours before cooling to 600 °C in 6 hours. After dwelling at 600 °C for 7 days, the ampoule was quenched into ice water and then cut into 1 mm thick slabs. X-ray diffraction confirmed that these pellets were nearly single phase  $\text{IrMn}_3$  with ordered Ir and Mn ions in the  $\text{AuCu}_3$  structure ( $Pm\bar{3}m$  space group), with no preferred crystal orientation and a  $\sim 8$  wt% MnO impurity fraction. Careful visual inspection of the pellets revealed that the MnO impurity was predominantly contained in a 0.1-mm-thick surface layer, corresponding to a 2 wt% MnO fraction in the bulk. While the MnO surface layer could be removed by carefully polishing the samples, this process also introduced significant Mn/Ir site disorder and therefore was abandoned.

#### B. Experimental details

INS experiments were performed on the direct-geometry time-of-flight (TOF) chopper spectrometer SEQUOIA [21,22] at Oak Ridge National Laboratory's Spallation Neutron Source. The 1-mm-thick  $\text{IrMn}_3$  slabs were laid in a closed packed array in a 1 mm thick flat plate Al cell. This arrangement minimizes Ir neutron absorption in the INS experiment. Spectra were collected with incident energies  $E_i = 50, 100, 200, 300,$  and  $500$  meV in coarse energy resolution mode (elastic resolution of  $\sim 4\%$   $E_i$ ) at  $T = 5$  K to investigate the spin wave excitations in the magnetically ordered phase. The incident energy for the measurements was selected by operating a Fermi chopper at various frequencies (240 Hz for  $E_i = 50$  or 100 meV, 420 Hz for  $E_i = 200$  meV, 480 Hz

for  $E_i = 300$  meV or 600 Hz for  $E_i = 500$  meV), and the background from the prompt pulse was removed with a  $T_0$  chopper operating at 60 Hz ( $E_i = 50$  or 100 meV), 120 Hz ( $E_i = 200$  or 300 meV) or 150 Hz ( $E_i = 500$  meV) [22]. An empty Al cell was measured in identical experimental conditions for the  $E_i = 50, 100, 200,$  and  $500$  meV cases. These resulting background spectra were subtracted from the corresponding sample spectra after applying the self-shielding correction (i.e., scale factor) required due to the strong neutron absorption of Ir. The scale factor was chosen by matching the Al Bragg peak intensities in the  $\text{IrMn}_3$  and empty cell spectra as closely as possible. No empty Al cell measurement was performed for  $E_i = 300$  meV since the corresponding  $\text{IrMn}_3$  data were only used to investigate magnetic excitations above the Al phonon density-of-states cutoff in this case.

#### C. Experimental results

The INS results are reduced from TOF and pixel position to  $Q$  and  $E$  using MANTID [23]. Various plots of the INS intensity were generated from these reduced data using DAVE [24]. The intensity is plotted as  $\frac{k_i}{k_f} \frac{\partial^2 \sigma}{\partial \Omega \partial E}$ , where  $k_i$  and  $k_f$  are the incident and final neutron momenta respectively and  $\frac{\partial^2 \sigma}{\partial \Omega \partial E}$  is the double differential cross-section for all scattering processes in the material. The magnetic scattering contribution to the intensity is proportional to the powder-averaged (magnetic) dynamical structure factor times the magnetic form factor squared.

The plots in Fig. 4 summarize some key results from the SEQUOIA experiment. Panels (a) and (b) depict the  $\text{IrMn}_3$  spectra collected with  $E_i = 100$  and  $500$  meV, respectively. Several prominent features are visible in this data. Most importantly, there are three nearly-vertical columns of scattering indicated by the arrows in Fig. 4(a). We attribute these columns of scattering to the signal of interest, the  $\text{IrMn}_3$  spin wave excitations, for several reasons: (i) they are centered above  $Q = 1.67, 2.36,$  and  $3.75/4.10 \text{ \AA}^{-1}$ , which correspond to the (100), (110), and (210)/(211) magnetic Bragg peak positions, (ii) their steeply-dispersive nature at low energies suggests a large excitation bandwidth, which is compatible with the high magnetic transition temperature, and (iii) the intensity of these columns of scattering decreases with increasing  $Q$ . The  $E_i = 500$  meV data allowed us to determine the magnetic excitation bandwidth for  $\text{IrMn}_3$ , which is essential information required to determine the exchange constants. The data presented in Fig. 4(b), combined with the  $E_i = 200$  and  $300$  meV data shown in Figs. 6(a) and 6(b), establish a value of  $E \sim 190$  meV for the top of the magnon band. Finally, we find that the spin wave excitations are characterized by a sizable energy gap, which is best illustrated by the  $E_i = 50$  meV color contour plot shown in Fig. 4(c) and the corresponding (100) constant- $Q$  cut presented in Fig. 4(d). There are also some notable background features in this data. Firstly, there is a strong phonon contribution between energy transfers  $E \sim 10 - 35$  meV. Secondly, there is a weakly dispersive magnetic mode between 10 and 18 meV covering a  $Q$  range of  $0.7 - 2.5 \text{ \AA}^{-1}$  that is consistent with a spin wave band from the small amount of MnO in our sample. Unfortunately, the presence of the MnO magnon mode precludes a precise

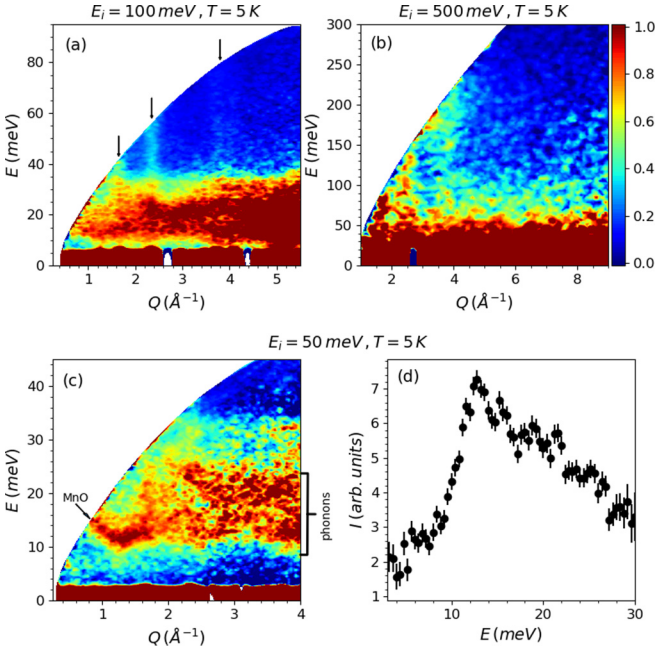


FIG. 4. (a)  $E_i = 100$  meV color contour plot from SEQUOIA. Three nearly vertical columns of scattering are visible in this spectrum and these features correspond to the IrMn<sub>3</sub> spin wave excitations. (b)  $E_i = 500$  meV color contour plot that illustrates the magnetic excitation band extends up to  $E \sim 190$  meV. (c)  $E_i = 50$  meV color contour plot. The vertical columns of scattering are also visible in these data, although they are difficult to detect due to the strong phonon background. Notably, the vertical columns of scattering do not extend down to the elastic line, which is indicative of a significant spin wave gap  $\Delta \geq 13$  meV. The precise value is difficult to determine due to the overlapping spin wave mode from the MnO impurity. (d) A constant- $Q$  cut centered about the (100) magnetic Bragg peak position (integration range of  $Q = [1.5, 1.9] \text{ \AA}^{-1}$ ) also shows strong evidence for a significant spin wave gap.

experimental determination of the spin gap for IrMn<sub>3</sub> and only allows us to place a lower bound of 13 meV on this value. Nevertheless, the observed gap is consistent with the DFT prediction of 17 meV.

#### D. Comparison with linear spin wave theory

To provide a quantitative comparison with the experimental data, the powder-averaged dynamical structure factor  $S(Q, \omega)$  times the magnetic form factor squared was calculated for various candidate spin wave models. More details of the  $S(Q, \omega)$  powder-averaging procedure are presented in Appendix B. The magnetic form factor, in the usual dipole or spherical approximation, is given by [25,26]:

$$f(s) = \langle j_0 \rangle = Ae^{-as^2} + Be^{-bs^2} + Ce^{-cs^2} + D, \quad (4)$$

where  $s = Q/4\pi$ . In principle, the values of the dimensionless constants depend on the oxidation state of Mn. Since an effective spin value of  $S = 1.33$  was incorporated in the DFT calculations, we used the  $A, a, B, b, C, c,$  and  $D$  parameters for the Mn<sup>4+</sup> form factor [26] throughout most of this work. Modifications from the Mn<sup>4+</sup> form factor were then considered in the INS data fitting process discussed later.

Figure 5 shows the calculated powder-averaged spin wave spectra for four candidate models. More specifically, the following scenarios were considered: (a) nearest neighbor exchange  $J_1$  only; (b) nonzero  $J_1$ , and  $J_2$ ; (c) nonzero  $J_1$ ,  $J_2$ , and  $J_3$ ; and (d) nonzero  $J_1$ ,  $J_2$ ,  $J_3$ , and  $J_4$ . Note that the last model uses the DFT values for the exchange constants reported in Ref. [10], while the exchange constants for the other three models were scaled to produce the  $E \sim 150$  meV excitation bandwidth that matches the  $J_1$ - $J_2$ - $J_3$ - $J_4$  model, with the  $J_2/J_1$  and  $J_3/J_1$  ratios fixed to the DFT values. All of the models include magnetic anisotropy  $K$ , which was also fixed to the value obtained from DFT calculations [18]. Notably, the vertical columns of magnetic scattering observed in the INS data shown in Fig. 4(a) can be used to help determine the most appropriate spin wave model for IrMn<sub>3</sub>. Figure 5 shows that these features are not well-defined in the NN only model and become more apparent as extended neighbor exchange interactions are added. Furthermore, the intensities of the  $Q = 1.67$  and  $2.36 \text{ \AA}^{-1}$  vertical columns of scattering become much more comparable in the  $J_1$ - $J_2$ - $J_3$  and  $J_1$ - $J_2$ - $J_3$ - $J_4$  models, which agrees well with the INS data. Consequently, the  $J_1$  only and  $J_1$ - $J_2$  models can be discarded.  $J_3$  and/or  $J_4$  seem to play an important role in producing the observed magnetic excitation spectrum.

Although the  $J_1$ - $J_2$ - $J_3$ - $J_4$  model is also supported by previous DFT work [10], it is clear that the experimental magnon bandwidth of 190 meV is much larger than the calculated value of 150 meV. Consequently, it is important to fit the INS data to the  $J_1$ - $J_2$ - $J_3$ - $J_4$  model to extract refined values for the exchange constants. We focused on the  $E_i = 200$  and 300 meV data with  $E \geq 80$  meV due to the significant phonon background at lower energy transfers and employed a three-step procedure using a  $\chi^2$  minimization routine with the cubic anisotropy  $K$  held fixed to the DFT value of 2.2 meV. We first found appropriate starting values for all four exchange constants by performing a fit of the constant- $Q$  cut (integration range  $[6.75, 7.25] \text{ \AA}^{-1}$ ) extracted from the  $E_i = 200$  meV dataset shown in Fig. 6(a), as this helped to establish an accurate magnon bandwidth. One defining feature of the IrMn<sub>3</sub> magnon spectrum is the double-peak structure near the top of the band, which is captured well by this fit. We have also overplotted a constant- $Q$  cut (integration range  $[4.75, 5.25] \text{ \AA}^{-1}$ ) of the  $E_i = 300$  meV data to illustrate that its intensity profile looks similar, but the double-peak structure is not as well-defined due to the coarser instrument energy resolution.

The next two steps involved fitting the intensity of the  $E_i = 300$  meV dataset as a function of both  $Q$  and  $E$ . First, we fixed the exchange constants to the values determined from the constant- $Q$  cut and considered modifications to the Mn<sup>4+</sup> form factor. The best fit was obtained by using the expression [27,28]:

$$f(s) = \langle j_0 \rangle + \left(1 - \frac{2}{g}\right) \langle j_2 \rangle, \quad (5)$$

with  $g = 1.22(5)$ . The values for  $\langle j_0 \rangle$  and  $\langle j_2 \rangle$  were obtained from the tabulated values for Mn<sup>4+</sup> [26]. Although our model used for the form factor includes terms that typically signify the importance of spin-orbit coupling and may have some merit for IrMn<sub>3</sub> [29], our current data can also

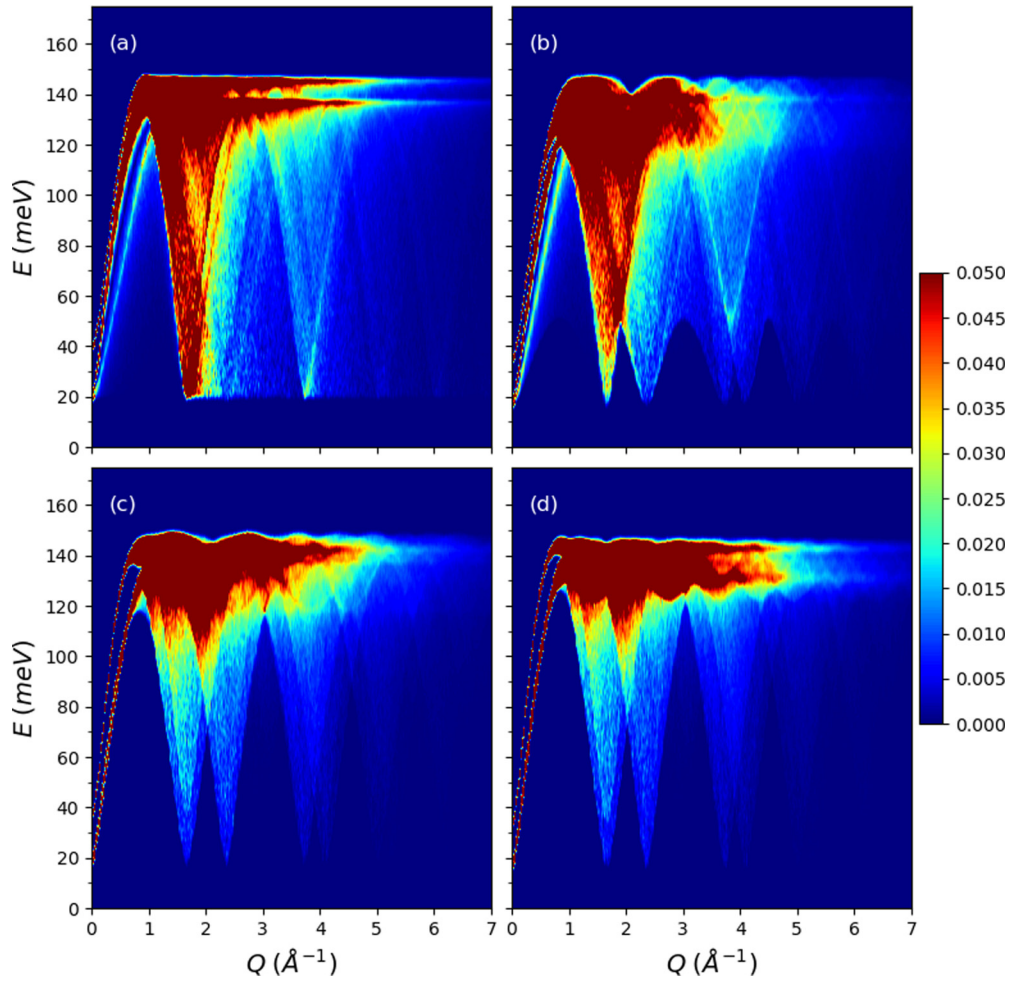


FIG. 5. Calculated, powder-averaged inelastic neutron scattering spectrum with magnetic anisotropy and (a) with nearest neighbor exchange  $J_1$  only, (b) with  $J_1$  and  $J_2$  only, (c) with  $J_1$ ,  $J_2$ , and  $J_3$  only, and (d) with the four exchange constants  $J_1$ ,  $J_2$ ,  $J_3$ , and  $J_4$  determined previously by DFT. The exchange constants for the three models shown in (a)–(c) were scaled to produce the  $\sim 150$  meV excitation bandwidth that matches the  $J_1$ - $J_2$ - $J_3$ - $J_4$  model, with the  $J_2/J_1$  and  $J_3/J_1$  ratios fixed to the DFT values.  $K$  was also fixed to the DFT value.

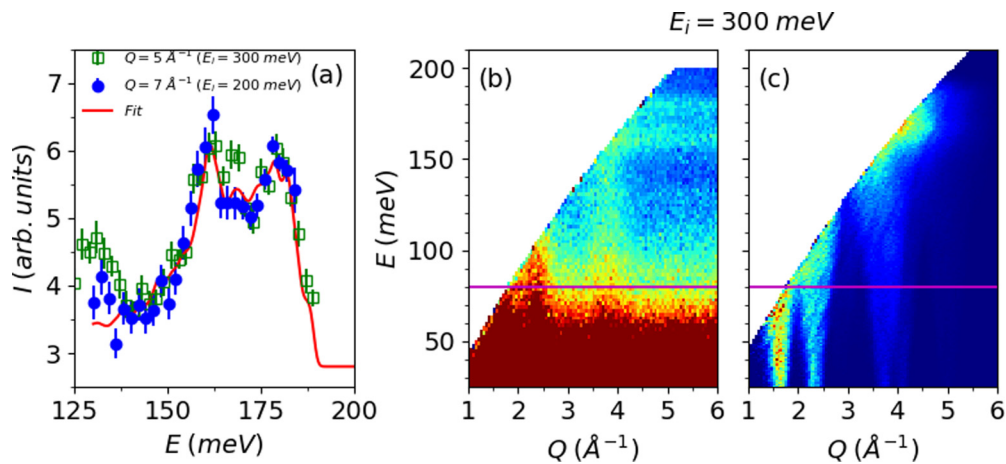


FIG. 6. (a) Constant- $Q$  cut of the  $E_i = 200$  meV data with an integration range  $[6.75, 7.25] \text{ \AA}^{-1}$ . The best fit to the  $J_1$ - $J_2$ - $J_3$ - $J_4$  model described in the text is superimposed on the data. A constant- $Q$  cut of the  $E_i = 300$  meV data with an integration range  $[4.75, 5.25] \text{ \AA}^{-1}$  are also shown to illustrate that its intensity profile is similar, but the double-peak structure near the top of the magnon band is not as well-resolved due to the coarser instrument energy resolution. (b) Color contour plot of the  $E_i = 300$  meV SEQUOIA data that illustrates a spin wave spectrum extending up to  $E \sim 190$  meV. (c) Color contour plot of the calculated powder-averaged magnetic excitation spectrum for  $\text{IrMn}_3$  with  $E_i = 300$  meV using the fitted Hamiltonian parameters described in the main text. The agreement with the data is excellent, which suggests that the  $J_1$ - $J_2$ - $J_3$ - $J_4$  model with cubic anisotropy is appropriate for  $\text{IrMn}_3$ .

be explained by small deviations from a completely localized model.

For the last step, we first fixed the parameters in the magnetic form factor expression to the values obtained just above and attempted to fit the 2D data by varying all four exchange constants simultaneously. Unfortunately, we found that this fit did not converge. The same problem was encountered when we let any three of the exchange constants vary and left the fourth parameter fixed. This may be due to the limited energy range available for fitting the data due to the strong phonon contributions below 80 meV. On the other hand, we found that the exchange parameters could be varied in pairs while the other two were held fixed. Therefore, we attempted to fit the data with all exchange parameter combinations that satisfied these convergence criteria. We found the greatest improvement in fit quality (i.e., smallest  $\chi^2$ ) when  $J_1$  and  $J_3$  were allowed to vary and  $J_2$  and  $J_4$  were held fixed to the values obtained in step 1 described above. This final fitting result yielded values of  $J_1 = 10.1(5)$  meV,  $J_2 = -3.3(2)$  meV,  $J_3 = 4.7(2)$  meV, and  $J_4 = -2.6(2)$  meV. Note that the uncertainty in each fit parameter is given by the difference in the best fit value and the value required to increase  $\chi^2$  by one for the 2D fit when the other parameters are held fixed.

A color contour plot of the calculated powder-averaged magnetic excitation spectrum for IrMn<sub>3</sub> using the fitted Hamiltonian parameters is presented in Fig. 6(c). We did not include scattering contributions from IrMn<sub>3</sub> phonons or the MnO impurity phase in this simulation as they contribute minimal scattering intensity above 80 meV, as shown in Fig. 6(b). Furthermore, the observed features from the spectrum are broader than the energy resolution of the instrument, as determined by both analytical calculations [22] and Monte Carlo ray tracing simulations with McVine [30], so this effect was not included in the simulation. Instrumental  $Q$  resolution was not considered here.

The simulation presented in Fig. 6(c) describes the data above energy transfers of 80 meV remarkably well. While this  $J_1$ - $J_2$ - $J_3$ - $J_4$  model itself has been proposed previously on the basis of DFT work [10] with values of  $J_1 = 11.6$  meV,  $J_2 = -1.5$  meV,  $J_3 = 3.2$  meV, and  $J_4 = -1.4$  meV, the exchange parameters found here are somewhat different. A comparison to the DFT results indicates that the best fit to the INS data yields a slightly smaller  $J_1$  and much larger values for the extended neighbor interactions; the latter are responsible for the increased experimental magnon bandwidth. This discrepancy between the experimental bandwidth and the calculated bandwidth from DFT is not well understood and should be investigated further in future work. Furthermore, the experimental intensity near the top of the magnon band extends out farther in  $Q$  than can be explained by the current model. This may arise from magnetovibrational coupling, but the precise origin of this behavior is beyond the scope of the present work.

#### IV. SUMMARY AND CONCLUSIONS

The geometry of ABC-stacked kagome planes in IrMn<sub>3</sub> offers a rare example to study a truly 3D frustrated kagome antiferromagnet. This material is also interesting for practical reasons, as it is a conductor that has been widely used as the exchange-pinning antiferromagnetic thin film in spin valve

technology. The so-called  $q = 0$  triangular spin structure is preserved in this 3D system along with some of the degeneracies of the NN Heisenberg model which stimulated previous work in the 2D case. A focus of the present results is to quantify the role of further-neighbor exchange interactions within a local-moment model of spin wave excitations in IrMn<sub>3</sub>, extending our earlier work that involved only NN exchange [12].

Inelastic neutron scattering data on a powder sample are also presented here. The observation of a large spin gap provides experimental evidence that magnetic anisotropy plays an important role in this material and provides strong motivation for revisiting the co-planar magnetic structure determined previously. Model calculations and inelastic neutron scattering data fitting show that the bandwidth, spectral weight, and spin gap of the magnetic excitation spectrum are best explained by a Hamiltonian including exchange interactions up to fourth nearest neighbor and strong cubic anisotropy, as originally determined by DFT.

The experimental verification of the large spin gap is an important result as our earlier work demonstrated that magnetic anisotropy induces a uniform magnetic moment along the [111] directions [11], which likely indicates an important mechanism for exchange coupling to adjacent ferromagnetic thin films. Such a uniform moment could also be employed to induce a single magnetic domain in field-cooled single crystal samples. Furthermore, the experimental verification of strong further-neighbor exchange interactions in IrMn<sub>3</sub>, which serve to further stabilize the  $q = 0$  spin structure, suggest that this state should be robust to thermal fluctuations and applied uniform magnetic fields. Such considerations are important in the design of magnetic information technology with ever diminishing dimensions and may provide some insight into the widespread utility of this compound in spin valves.

#### ACKNOWLEDGMENTS

This work was supported by the Natural Sciences and Engineering Council (NSERC) of Canada, the Canada Foundation for Innovation (CFI), and Compute Canada. Materials synthesis by JQY was supported by the US Department of Energy, Office of Science, Basic Energy Sciences, Materials Sciences and Engineering Division. A portion of this research used resources at the Spallation Neutron Source, a DOE Office of Science User Facility operated by Oak Ridge National Laboratory (ORNL). The Monte Carlo ray tracing simulations were performed on the CADES cloud computing resource at ORNL.

#### APPENDIX A: ADDITIONAL DETAILS FOR MODEL RESULTS

As described in I, in the absence of anisotropy, spins are coplanar with zero net magnetization. Anisotropy serves to lift the spin vectors out of the plane and induce a finite magnetization in a  $\langle 111 \rangle$  direction [11]. This effect is characterized by  $\alpha$ , the angle between each sublattice spin and its anisotropy axis [ $\alpha = \cos(\mathbf{S}_i \cdot \mathbf{n}_i)$ ,  $i = A, B, C$ ], and  $\beta$ , the angle with respect to the other two anisotropy axes [ $\beta = \cos(\mathbf{S}_i \cdot \mathbf{n}_j)$ ,  $i \neq j$ ], where  $\alpha^2 + 2\beta^2 = 1$ . The modified ground state

energy per spin that includes further-neighbor exchange is given by [compare Eqs. (2) and (3) in I] where  $S = 1$  is used for convenience as in I

$$E/N = 4(J_1 + 2J_3)(\beta^2 - 2\alpha\beta) - K\alpha^2 + 3J_2 + 6J_4 \quad (\text{A1})$$

and is minimized when  $\alpha$  has the value

$$\alpha = \sqrt{1/2 + 1/2\sqrt{1 - 1/[1 + (\tilde{K} + 1)^2/8]}}, \quad (\text{A2})$$

$$-i\omega \begin{pmatrix} \tilde{S}_A^x \\ \tilde{S}_B^x \\ \tilde{S}_C^x \\ \tilde{S}_A^y \\ \tilde{S}_B^y \\ \tilde{S}_C^y \end{pmatrix} = \begin{pmatrix} 0 & Y_{AB} & -Y_{AC} & X & Z_{AB} & Z_{AC} \\ -Y_{AB} & 0 & Y_{BC} & Z_{AB} & X & Z_{BC} \\ Y_{AC} & -Y_{BC} & 0 & Z_{AC} & Z_{BC} & X \\ W & T_{AB} & T_{AC} & 0 & Y_{AB} & -Y_{AC} \\ T_{AB} & W & T_{BC} & -Y_{AB} & 0 & Y_{BC} \\ T_{AC} & T_{BC} & W & Y_{AC} & -Y_{BC} & 0 \end{pmatrix} \begin{pmatrix} \tilde{S}_A^x \\ \tilde{S}_B^x \\ \tilde{S}_C^x \\ \tilde{S}_A^y \\ \tilde{S}_B^y \\ \tilde{S}_C^y \end{pmatrix}, \quad (\text{A3})$$

where  $Y$ ,  $T$ , and  $Z$  are defined in I and with the following modifications:

$$\begin{aligned} X &= [8(J_1 + 2J_3)(\beta - 2\alpha)\beta - 2K\alpha^2 \\ &\quad + 6J_2 - 2J_2(\cos Q_x a + \cos Q_y a + \cos Q_z a) \\ &\quad + 12J_4 - 4J_4(\cos Q_x a \cos Q_y a + \cos Q_x a \cos Q_z a \\ &\quad + \cos Q_y a \cos Q_z a)], \\ W &= [8(J_1 + 2J_3)(2\alpha - \beta)\beta + 2K(\alpha^2 - 2\beta^2) \\ &\quad - 6J_2 + 2J_2(\cos Q_x a + \cos Q_y a + \cos Q_z a) \\ &\quad - 12J_4 + 4J_4(\cos Q_x a \cos Q_y a + \cos Q_x a \cos Q_z a \\ &\quad + \cos Q_y a \cos Q_z a)], \end{aligned} \quad (\text{A4})$$

and

$$\begin{aligned} \lambda_{AB} &= 4[J_1 + 2J_3 \cos Q_z a] \cos(\tfrac{1}{2}Q_x a) \cos(\tfrac{1}{2}Q_y a), \\ \lambda_{BC} &= 4[J_1 + 2J_3 \cos Q_y a] \cos(\tfrac{1}{2}Q_x a) \cos(\tfrac{1}{2}Q_z a), \\ \lambda_{AC} &= 4[J_1 + 2J_3 \cos Q_x a] \cos(\tfrac{1}{2}Q_y a) \cos(\tfrac{1}{2}Q_z a), \end{aligned} \quad (\text{A5})$$

where coordinates are in terms of cube axes with lattice constant  $a$ . Note that for the spin-wave frequency, the bare exchange and anisotropy constants are divided by  $S$ .

In the absence of anisotropy, the case  $K = 0$ , the eigenvalue problem involves the  $3 \times 3$  symmetric matrix Eq. (7) in I with elements now given by

$$\begin{aligned} A_1 &= X^2 - (\lambda_{AB}^2 + \lambda_{AC}^2)/2, \\ A_2 &= X^2 - (\lambda_{AB}^2 + \lambda_{BC}^2)/2, \\ A_3 &= X^2 - (\lambda_{AC}^2 + \lambda_{BC}^2)/2, \\ B_1 &= -X\lambda_{AB}/2 - \lambda_{AC}\lambda_{BC}/2, \\ B_2 &= -X\lambda_{AC}/2 - \lambda_{AB}\lambda_{BC}/2, \\ B_3 &= -X\lambda_{BC}/2 - \lambda_{AB}\lambda_{AC}/2. \end{aligned} \quad (\text{A6})$$

where  $\tilde{K} = K/(2J_1 + 4J_3)$  and  $\beta = \sqrt{1-\alpha^2}$  using the positive values of the square roots to give physical solutions. Note that there are eight degenerate ground states corresponding to the eight (111) axes [11]. The analysis of spin excitations in this section correspond to a single domain [111] crystal.

The basic structure of the linearized spin wave theory presented in I remains the same with further-neighbor exchange added. The  $6 \times 6$  matrix characterizing dynamic fluctuations of the transverse spin components in a local coordinate system is again given by

The special case  $Q_x = Q_y = Q_z$  again yields eigenvalues of the general form given by Eq. (11) in I but further reduction in terms of the  $J_i$  is not illuminating. However, for the case where the wave vector is directed along a cube axis,  $Q_y = Q_z = 0$ , for example, it can be shown that one of the three modes takes the form

$$\begin{aligned} \omega_1^2 &= (2J_2 + 8J_4 - 8J_3)[(6J_1 + 12J_3)(\cos Q_x a - 1) \\ &\quad + (2J_2 + 8J_4 + 4J_3)(\cos Q_x a - 1)^2]. \end{aligned} \quad (\text{A7})$$

This yields the zero energy mode [see Eq. (13) of I] in the absence of further-neighbor exchange. It is also zero if  $2J_2 + 8J_4 = 8J_3$ , which is not possible in the case of  $\text{IrMn}_3$  with  $J_3 > 0$  and  $J_2, J_4 < 0$ . Thus, as in the 2D case, further-neighbor exchange removes the flat mode.

## APPENDIX B: ADDITIONAL DETAILS FOR INELASTIC NEUTRON SCATTERING

For comparison of the calculated dynamical structure factor with the experimental INS data,  $S(\mathbf{Q}, \omega)$  is averaged over all crystallographic directions, yielding

$$S(Q, \omega) = \int_{\phi=0}^{2\pi} \int_{\theta=0}^{\pi} S(\mathbf{Q}, \omega) \sin \theta \, d\theta \, d\phi, \quad (\text{B1})$$

where  $\theta$  and  $\phi$  are the azimuthal and polar angles describing the orientation of  $\mathbf{Q}$ . This integral can be approximated through Monte Carlo integration using the following expression:

$$S(Q, \omega) = \frac{1}{n} \sum_{i=1}^n S(Q, \arccos(2a_i - 1), 2\pi b_i, \omega). \quad (\text{B2})$$

In the equation above,  $a$  and  $b$  represent two random numbers from 0 to 1 and  $n$  is the number of iterations. Typically, 1000 random directions are chosen for each  $Q$ .

- [1] V. Hemmati, M. L. Plumer, J. P. Whitehead, and B. W. Southern, *Phys. Rev. B* **86**, 104419 (2012).
- [2] J. T. Chalker, P. C. W. Holdsworth, and E. F. Shender, *Phys. Rev. Lett.* **68**, 855 (1992).
- [3] A. B. Harris, C. Kallin, and A. J. Berlinsky, *Phys. Rev. B* **45**, 2899 (1992).
- [4] S. Schnabel and D. P. Landau, *Phys. Rev. B* **86**, 014413 (2012).
- [5] K. Matan, D. Grohol, D. G. Nocera, T. Yildirim, A. B. Harris, S. H. Lee, S. E. Nagler, and Y. S. Lee, *Phys. Rev. Lett.* **96**, 247201 (2006).
- [6] K. O'Grady, L. E. Fernandez-Outon, and G. Vallejo-Fernandez, *J. Magn. Magn. Mater.* **322**, 883 (2010).
- [7] M. Tsunoda, H. Takahashi, T. Nakamura, C. Mitsumata, S. Isogami, and M. Takahashi, *Appl. Phys. Lett.* **97**, 072501 (2010).
- [8] A. Kohn, A. Kovacs, R. Fan, G. J. McIntyre, R. C. C. Ward, and J. P. Goff, *Sci. Rep.* **3**, 2412 (2013).
- [9] R. Yanes, J. Jackson, L. Udvardi, L. Szunyogh, and U. Nowak, *Phys. Rev. Lett.* **111**, 217202 (2013).
- [10] L. Szunyogh, B. Lazarovits, L. Udvardi, J. Jackson, and U. Nowak, *Phys. Rev. B* **79**, 020403(R) (2009).
- [11] M. D. LeBlanc, M. L. Plumer, J. P. Whitehead, and B. W. Southern, *Phys. Rev. B* **88**, 094406 (2013).
- [12] M. D. LeBlanc, B. W. Southern, M. L. Plumer, and J. P. Whitehead, *Phys. Rev. B* **90**, 144403 (2014).
- [13] H. V. Yerzhakov, M. L. Plumer, and J. P. Whitehead, *J. Phys.: Condens. Matter* **28**, 196003 (2016).
- [14] Krén, G. Kádár, L. Pál, J. Sólyom, and P. Szabó, *Phys. Lett.* **20**, 331 (1966); E. Krén, G. Kádár, L. Pál, J. Sólyom, P. Szabó, and T. Tarnóczy, *Phys. Rev.* **171**, 574 (1968); A. Sakuma, R. Y. Umetsu, and K. Fukamichi, *Phys. Rev. B* **66**, 014432 (2002); T. Ikeda and Y. Tsunoda, *J. Phys. Soc. Jpn.* **72**, 2614 (2003).
- [15] I. Tomeno, H. N. Fuke, H. Iwasaki, M. Sahashi, and Y. Tsunoda, *J. Appl. Phys.* **86**, 3853 (1999).
- [16] T. Kaneko, T. Kanomata, and K. Shirakawa, *J. Phys. Soc. Jpn.* **56**, 4047 (1987); K. Takenaka, T. Inagaki, and H. Takagi, *Appl. Phys. Lett.* **95**, 132508 (2009); Y. Sun, Y. Guo, Y. Tsujimoto, J. Yang, B. Shen, W. Yi, Y. Matsushita, C. Wang, X. Wang, J. Li, C. L. Satish, and K. Yamaura, *Inorg. Chem.* **52**, 800 (2013).
- [17] L. Szunyogh and U. Nowak (private communication).
- [18] L. Szunyogh, L. Udvardi, J. Jackson, U. Nowak, and R. Chantrell, *Phys. Rev. B* **83**, 024401 (2011).
- [19] T. Uchida, Y. Kakehashi, and N. Kimura, *J. Magn. Magn. Mater.* **400**, 103 (2016).
- [20] W. Marshall and S. W. Lovesey, *Theory of Thermal Neutron Scattering* (Clarendon Press, Oxford, 1971).
- [21] G. E. Granroth, D. H. Vandergriff, and S. E. Nagler, *Phys. B: Condens. Matter* **385–386**, 1104 (2006).
- [22] G. E. Granroth, A. I. Kolesnikov, T. E. Sherline, J. P. Clancy, K. A. Ross, J. P. C. Ruff, B. D. Gaulin, and S. E. Nagler, *J. Phys.: Conf. Ser.* **251**, 012058 (2010).
- [23] O. Arnold, J. C. Bilheux, J. M. Borreguero, A. Buts, S. I. Campbell, L. Chapon, M. Doucet, N. Draper, R. Ferraz Leal, M. A. Gigg, V. E. Lynch, A. Markvardsen, D. J. Mikkelsen, R. L. Mikkelsen, R. Miller, K. Palmen, P. Parker, G. Passos, T. G. Perring, P. F. Peterson, S. Ren *et al.* *Nucl. Instrum. Methods A* **764**, 156 (2014).
- [24] R. T. Azuah, L. R. Kneller, Y. Qiu, P. L. W. Tregenna-Piggott, C. M. Brown, J. R. D. Copley, and R. M. Dimeo, *J. Res. NIST* **114**, 341 (2009).
- [25] J. T. Haraldsen and R. S. Fishman, and G. Brown, *Phys. Rev. B* **86**, 024412 (2012).
- [26] P. J. Brown,  $j_0$  form factors for 3d transition elements and their ions, <https://www.ill.eu/sites/ccsl/ffacts/ffactnode5.html>, 1998.
- [27] R. J. Weiss and A. J. Freeman, *J. Phys. Chem. Solids* **10**, 147 (1959).
- [28] H. A. Mook, *Phys. Rev.* **148**, 495 (1966).
- [29] H. Chen, T.-C. Wang, D. Xiao, G.-Y. Guo, Q. Niu, and A. H. MacDonald, *Phys. Rev. B* **101**, 104418 (2020).
- [30] J. Y. Y. Lin, H. L. Smith, G. E. Granroth, D. L. Abernathy, M. D. Lumsden, B. Winn, A. A. Aczel, M. Aivazis, and B. Fultz, *Nucl. Instrum. Methods A* **810**, 86 (2016).